ACS APPLIED ENERGY MATERIALS

Article

Engineering of a Mo/SiN diffusion barrier to reduce the formation of MoS in CuZnSnS thin film solar cells

Zhengfei Wei, Chung Man Fung, Adam Pockett, Tom O. Dunlop, James D. McGettrick, Peter Heard, Owen J. Guy, Matthew Carnie, James Sullivan, and Trystan M. Watson

ACS Appl. Energy Mater., **Just Accepted Manuscript** • DOI: 10.1021/acsaem.8b00401 • Publication Date (Web): 22 May 2018

ACS Publications

is published by the American Chemical Society. 1155 Sixteenth Street N.W., Washington, DC 20036

Engineering of a Mo/Si_xN_y Diffusion Barrier to Reduce the Formation of MoS_2 in Cu_2ZnSnS_4 Thin Film Solar Cells

Zhengfei Wei[1*], Chung Man Fung[2], Adam Pockett[1], Tom Dunlop[1], James D. McGettrick[1], Peter Heard[3], Owen J. Guy[2], Matthew J. Carnie[1], James Sullivan[1] and Trystan M. Watson[1*]

[1]SPECIFIC, College of Engineering, Swansea University, Bay Campus, Swansea, SA1 8EN
[2]Centre of NanoHealth (CNH), College of Engineering, Swansea University, Singleton Campus, Swansea, SA2 8PP
[3]Interface Analysis Centre, University of Bristol, Tyndall Avenue, Bristol, BS8 1TL, UK
[*]Corresponding Authors: Zhengfei.Wei@swansea.ac.uk and T.M.Watson@swansea.ac.uk

Keywords: CZTS, interface recombination, MoS_2, TPV, solar cell and Si_xN_y.

ABSTRACT: The optimisation of the interface between back contact and absorber is one of the main challenges to improve the electrical behaviour and further enhance the efficiencies of $Cu_2ZnSn(S,Se)_4$ (CZTS(e)) solar cell devices. In this work, Mo/Si_xN_y thin films with various film thicknesses were introduced as an interfacial layer to explore its influence on opto-electronic properties of the pure sulphide CZTS thin film solar cells. The Si_xN_y was deposited through plasma enhanced chemical vapour deposition (PECVD). The film thickness and stress of the Mo/Si_xN_y films were controlled to improve the adhesion of the CZTS layer and reduce the chances of cracking the deposited films. Energy dispersive X-Ray spectroscopy (EDS) mapping measurements performed directly on the cross-section of Mo/Si_xN_y/CZTS/Mo films indicate that the Si_xN_y intermediate layer can effectively inhibit the formation of a highly resistive MoS_2 layer and decomposition of CZTS at the CZTS/Molybdenum (Mo) interface region. A reduced efficiency was obtained with a Si_xN_y modified back contact compared with the devices without this layer. This could be due to the increased recombination and poor hole extraction stemming from the very low valance band maximum of Si_xN_y obtained from ultraviolet photoelectron spectroscopy (UPS) measurements. Temperature dependent current density-voltage (T-JV) and temperature dependent transient photovoltage (T-TPV) measurements were used to uncover insights into the internal recombination dynamics of the charge carriers.

INTRODUCTION

Pure sulphide CZTS thin film solar cells have been extensively studied in the last few years as an earth-abundant and environmentally-friendly alternative to well-established $Cu(In,Ga)(Se,S)_2$ (CIGS) technologies.[1-3] Pure sulphide CZTS is an attractive earth-abundant, environmental-friendly and stable light harvesting photovoltaic material. The bandgap of pure sulphide CZTS is around 1.5 eV, which is close to the optimal bandgap required for a single junction solar cell. However, the record power conversion efficiency of these pure sulphide CZTS solar cells and toxic selenium-containing CZT(S, Se) solar cells have been stagnant at around 9% and 12.6% for a few years, mainly due to a large V_{oc} deficit. [4-5] Several factors has been proposed to explain this V_{oc} deficit, including, an unfavourable thick MoS_2 layer at the back contact [6], existence of charged defects associated with band tailing states [7], improper band alignment at the CZTS/CdS heterojunction interface [3]. To form a

phase-pure CZTS(e) material with relatively large grains, a high temperature (>500 °C) sulfurization annealing step is essential and unavoidable. This would normally lead to the formation of $MoS(e)_2$ between Mo and CZTS(e). The functionality of this $MoS(e)_2$ is still debatable as it greatly depends on the thickness of the layer. A very thin layer of $MoS(e)_2$ may help to form a quasi-ohmic contact at the interface and improve the adhesion of CZTS(e) on Mo.[8-9] However, it is likely to form a quite thick layer in the absence of sulphur or selenium excess (low partial pressure) during high temperature annealing along with the decomposition of CZTS into secondary phases (e.g. SnS, ZnS), which could increase the series resistance and therefore is detrimental for solar cell performance.[6, 8, 10] To address this issue, an effective barrier layer was introduced to prevent the formation of thick $MoS(e)_2$. To optimise the design of the back contact, several successful strategies have been successfully implemented to reduce the series resistance and increase the fill factor including Ag with good conductivity and additional p-type doping [11], ZnO[12-13], MoO_2[14] with good chemical stability; TiN[8, 15-16] and TiB_2 [9] with both good chemical stability and electrical conductivity. More recently, bilayer structures SiC/Mo[17] and Au/MoO_3[18] were reported to mainly boost the open circuit voltage and hence improve the power conversion efficiency.

Si_xN_y is a dielectric material with excellent chemical and thermal stability [19] and has been used as an antireflection coating (ARC) as well as a moisture barrier for crystalline silicon [20] and CIGS solar cells[21]. In this work, we employed a Mo/Si_xN_y diffusion barrier to avoid sulfurization of Mo and decomposition of CZTS. Due to the high resistivity of Si_xN_y, a further very thin layer of Mo (10-30 nm) was coated on top of Si_xN_y. We demonstrated the importance of controlling residual stress in back contact design to improve the adhesion of CZTS on the back surface. The influence of the Mo/Si_xN_y diffusion barrier on the materials quality and device performance of solar cells is presented.

EXPERIMENTAL SECTION

To design a suitable back contact for solution processed CZTS, a series of surface treatments and coatings were performed on the Mo/soda-lime glass (SLG) substrates. Oxygen plasma treatment was used to remove any surface contamination and improve wetting of DMSO based C-Z-T-S solutions onto the Mo surface. All the precursor solution were doped with 0.14M NaCl. In this work, we employed a 10 nm-thick silicon nitride Si_xN_y layer using a PECVD method directly on top of the Mo back contact. Si_xN_y is a thermally and chemically stable material, which would serve as an appropriate barrier layer to reduce the sulfurization of Mo. DMSO-based solutions showed very poor wettability onto the Si_xN_y surface. Therefore in addition to the high resistivity of Si_xN_y, a 10-30 nm thick Mo capping layer were sputtered on top of the Si_xN_y layer. The additional Mo layer provide improved conductivity and adhesion of CZTS in comparison to the plain Si_xN_y layer. Furthermore, the effect of the MoS_2 thickness formed between Si_xN_y and CZTS was investigated. The CZTS layers were deposited on these Mo/Si_xN_y modified back contacts by spin-coating of C-Z-T-S solution precursors and subsequently sulfurized in a rapid thermal processing (RTP, MTI Corporation) furnace at 560 °C for 20 mins. The solution preparation details are the same as those reported earlier. [22] The thickness of the CZTS absorbers was 1.2-1.3 μm. After coating CZTS layers, a ~70nm thick CdS layer was deposited by chemical bath deposition. Sputtered

intrinsic ZnO (~50 nm) and Sn:In_2O_3 (~350 nm) served as a transparent conductive oxide. A Ni-Al metal grid was deposited using thermal evaporation to improve the conductivity of the device.

The morphology of films was studied using a JEOL-JSM-7800F field emission scanning electron microscope (5 kV acceleration voltage, a working distance of 10 mm and a magnification of x 25, 000). Energy dispersive X-ray spectroscopy (EDX) mapping was used to deduce the element distribution using 20 kV acceleration voltage. The stress measurements were made with a Bruker D8 Discover X-ray diffraction system with a 0.07 ° step size, at a time of 7 seconds per step. The undertaken scans were over the full 0-0.9 $sin^2(\psi)$ in both positive and negative ψ tilts to confirm the absence of shear stress. Secondary ion mass spectrometry (SIMS) depth profiles were obtained using an in-house instrument constructed at the Interface Analysis Centre, University of Bristol, comprising of an electronically variable aperture type gallium ion gun (FEI SD gallium LMIS EVA focusing column) fitted to a double focusing magnetic sector mass analyser (Vacuum Generators model 7035). Surface spectra were obtained by scanning a 25 keV gallium ion beam over an area of the sample while scanning the magnet to accept secondary ions in the range 0-125 Daltons, with a step size of 0.05 Daltons and a dwell time of 100 ms per step. Hence a total time of 200 s to obtain the spectrum. Depth profiles were obtained by scanning a 3 nA gallium ion beam over an area of 43 μm x 43μm or 65 μm x 65μm and monitoring the species of interest. Sodium, silicon, copper, zinc, molybdenum and tin signals were counted with dwell times of 1s each, cycling through the elements for a total period of 20 minutes. The system vacuum during operation was 2 x 10^{-8} mbar. The instrument was calibrated using values of 68.93 for the backscattered Ga+ ions. The instrument control software was 'Pisces' running under the Windows operating system.[23] UPS was performed alongside XPS in the Kratos Axis Supra, utilising the He(I) line with a pass energy of 10 eV, step size of 0.025 eV and a 65 ms dwell. A 110 μm aperture was utilised in order to prevent saturation of the detector. The secondary electron cut-off and valence band edges were estimated using the Step Up and Step Down edge backgrounds within CasaXPS. In each case the measured value is the intersection of the step with the background electron counts. The current-density-voltage (J-V) curves for the solar cell devices were measured under simulated AM 1.5G spectrum and 100 mW/cm^2 (1 sun) illumination. The external quantum efficiency (EQE) measurements were performed in AC mode with a chopping frequency of 67 Hz using a QEX10 system (PV Measurements) calibrated with a NIST-certified Si photodiode. Transient photovoltage measurements were performed using a commercially available transient measurement system (Automatic Research GmbH). This system uses a 635 nm red laser diode driven by a waveform generator (Keysight 33500B). The laser pulse length was 100 ns. Background illumination was provided by a white LED with its intensity calibrated to generate the same device photocurrent as measured using the solar simulator. This intensity is referred to as 1 Sun equivalent. Transient responses were captured by a digital storage oscilloscope (Keysight DSOX2024A), the number of sample averages being adjusted to optimise signal noise and measurement time. The device under test is assumed to be held at open-circuit by the 1 MΩ oscilloscope input. TPV decays were fitted using a single exponential function. Temperature

dependent J-V and TPV measurements were performed using a temperature-controlled chamber (Linkam) under liquid nitrogen cooling.

RESULTS AND DISCUSSION

Since Si_xN_y and CZTS were prepared at 400 ºC and 560 ºC respectively, thermal effects would further enhance the stress variation which was indicated by CZTS film delamination in a previous publication[24]. Therefore, proper control on the stress is important for the back contact design. To determine the residual stress in multiple layer coatings, XRD was used to measure the peak shift on the diffraction pattern associated with inter-planar spacing *d* with relation to ψ angle. Strain causing elongation or contraction of the crystal lattice will induce the change in *d*, which could be obtained on the diffraction pattern. In this work, the $Sin^2\psi$ plot was used to derive the residual stress σ using Equation 1:

$$\sigma = \frac{E}{(1+\nu)sin^2\psi}\left(\frac{d_\psi - d_n}{d_n}\right) \quad \text{Equation 1}$$

where the inter-planar spacing of planes normal to the surface d_n, the inter-planar spacing of planes at an angle ψ to the surface d_ψ, Elastic modulus E and Poisson's ratio.[25] A number of XRD measurements were made at different psi (ψ) tilts for the Mo cleaned, plasma treated, Si_xN_y, Si_xN_y coating with 10 nm, 20 nm and 30 nm Mo-capping as shown Figure 1. The calculated stress values extracted from Figure 1 for the individual modifications of the back contact were plotted in Figure 2. The bottom Mo film was cleaned with DI water and IPA, the residual stress is estimated as -492.4±46.5 Mpa, which was used as a baseline for all the stress measurements. After 10 minutes O_2 plasma cleaning on the Mo surface, a dramatic increase in the compressive stress is derived as -885.1±37.8 Mpa. As we observed a better wetting after O_2 plasma cleaning, this dramatic increase of the compressive stress could be a good indication for improved film adhesion. However, a pronounced reduction of the compressive stress can be calculated as -730.4±62.6 Mpa after Si_xN_y coating. Changes in the mechanical property of the materials or the Mo/Si_xN_y stacked layers may contribute to the delamination of suphurised CZTS films and poor wetting of the C-Z-T-S solution on Si_xN_y surface. A significant increase in compressive stress after sputtering of the 10-30 nm Mo capping layer is estimated in the range of -1040 to -1000 Mpa. Improved wetting of the C-Z-T-S solution and CZTS film adhesion onto the Si_xN_y surface was obtained whilst in this stress range.

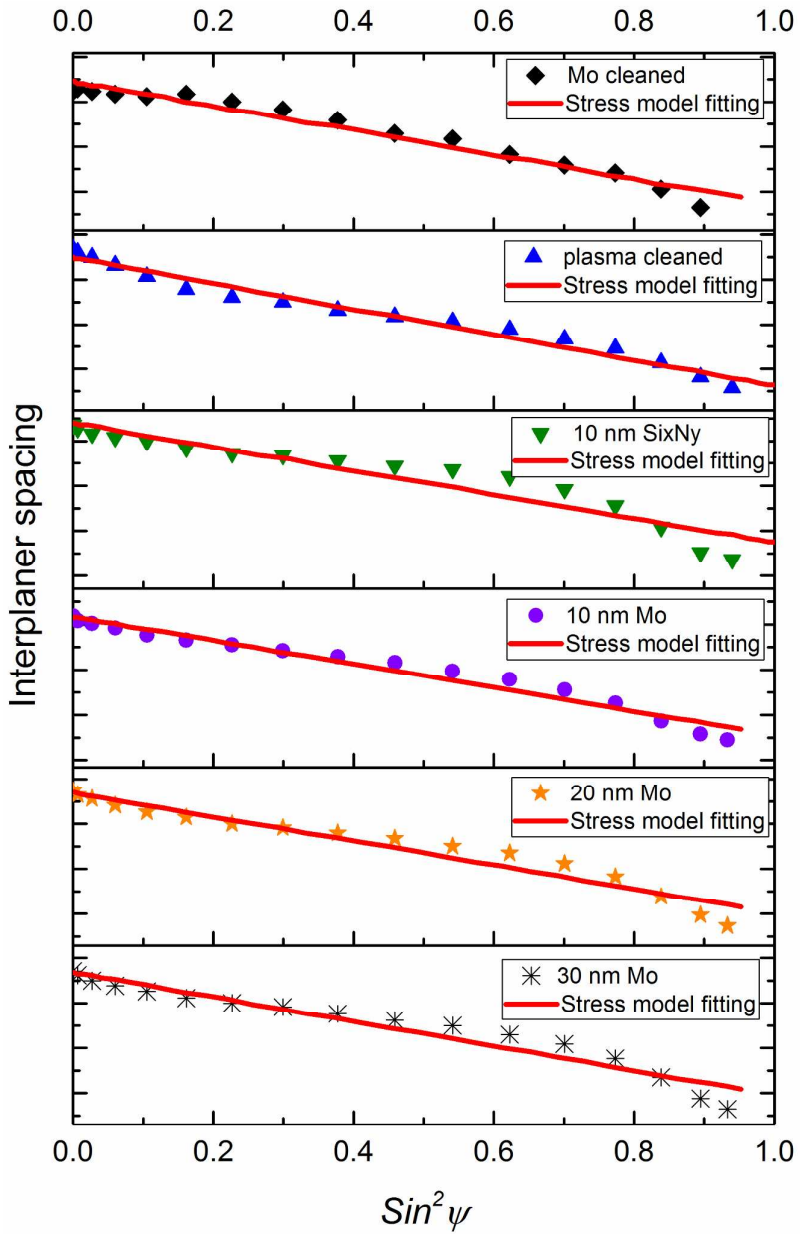

Figure 1. $Sin^2\psi$ plot of experimental and modelled results of various back contact configurations (untreated Mo, plasma cleaned Mo, 10nm-Si_xN_y/Mo/SLG, 10nm-Mo/10nm-Si_xN_y/Mo/SLG, 20nm-Mo/10nm-Si_xN_y/Mo/SLG, 30nm-Mo/10nm-Si_xN_y/Mo/SLG)

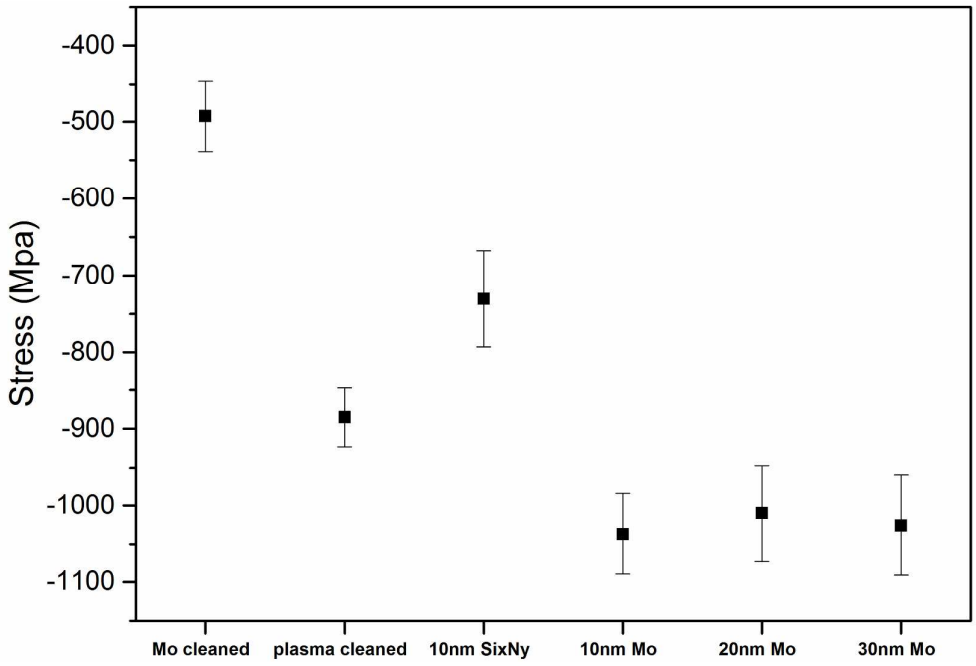

Figure 2. Residual stress of various back contact configurations (untreated Mo, plasma cleaned Mo, 10nm-Si_xN_y/Mo/SLG, 10nm-Mo/10nm-Si_xN_y/Mo/SLG, 20nm-Mo/10nm-Si_xN_y/Mo/SLG, 30nm-Mo/10nm-Si_xN_y/Mo/SLG)

After tuning the individual deposition parameters for Si_xN_y and Mo capping layers, the stress mismatch between the CZTS and back contacts was improved. To investigate the effectiveness of Si_xN_y and Mo capping layers as a sulphurisation barrier, cross-section SEM and EDS mapping were used to characterise CZTS samples with and without barrier layers (Figure 3). CZTS with good adhesion were obtained on Mo-capping/Si_xN_y as shown in Figure 3A1-3D1. CZTS films grown directly onto the Si_xN_y surface were non-uniform due to poor wetting and adhesion. The CZTS films with the Mo-capping/Si_xN_y barrier layers (Figure 3B1, 3C1 and 3D1) show a slightly bigger grain size than those without barrier layers (Figure 3A1). No significant differences in the film thickness and film compactness were found in these films. Figure 3A2 shows a sulphur distribution into the underlying Mo layer which could be an indication of MoS_2 formation. For the samples with barrier layers, a clear interface was created between sulphur and silicon and very little sulphur was detected within the Mo region (Figure 3B2, 3C2 and 3D2). The Mo-capping/Si_xN_y bilayer is shown to reduce or avoid the formation of MoS_2 at the back contact.

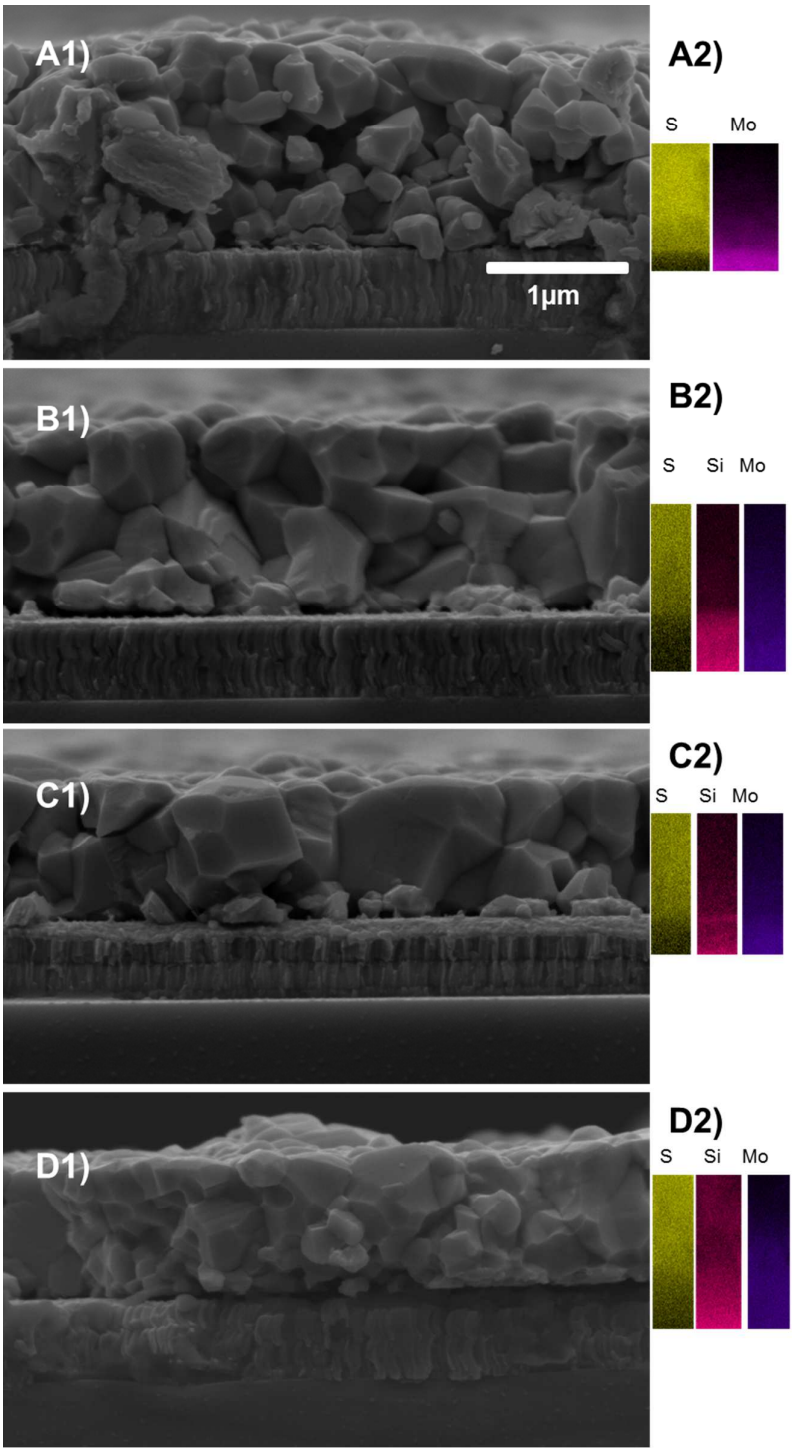

Figure 3. Cross-section SEM images of CZTS samples on Mo/SLG with or without barrier layers: A1) CZTS/Mo/SLG, A2) EDS mapping of a select area from SEM image A1); B1) CZTS/10nm-Mo/10nm-Si_xN_y/Mo/SLG, B2) EDS mapping of a select area from SEM image B1); C1) CZTS/20nm-Mo/10nm-Si_xN_y/Mo/SLG, C2) EDS mapping of a select area from SEM image C1); D1) CZTS/10nm-Mo/30nm-Si_xN_y/Mo/SLG, D2) EDS mapping of a select area from SEM image D1). The selected the elements in EDS mapping are labelled as yellow for S, purple for Mo and red for Si.

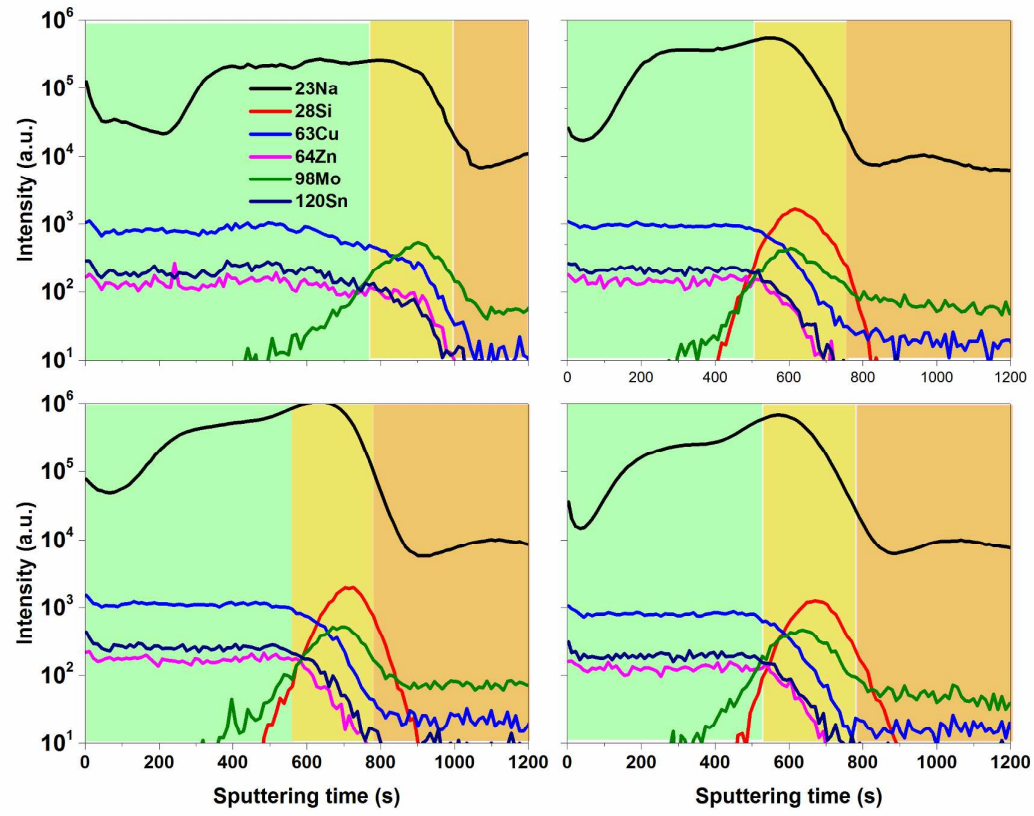

Figure 4. SIMS elemental depth profiles of CZTS samples on Mo/SLG with or without barrier layers: A) CZTS/Mo/SLG, B) CZTS/10nm-Mo/10nm-Si_xN_y/Mo/SLG, C) CZTS/20nm-Mo/10nm-Si_xN_y/Mo/SLG, D) CZTS/10nm-Mo/30nm-Si_xN_y/Mo/SLG. CZTS, MoS_2/Si_xN_y and Mo were showed with green, yellow and orange backgrounds, respectively.

From the SIMS depth profiles (Figure 4), there isn't significant difference on the depth profiles of Na due to intentionally doped all CZTS precursors with 0.14M NaCl. However, there is an apparent reduction of the Mo diffusion length after Mo/Si_xN_y barrier was added in Sample B-D. The slight variation of Mo intensity could be due to the varied thickness of MoS_2 formed towards the Si_xN_y surface. Further investigation with TEM/EDS would be required to analyse the interfaces in nm/sub-nm level.

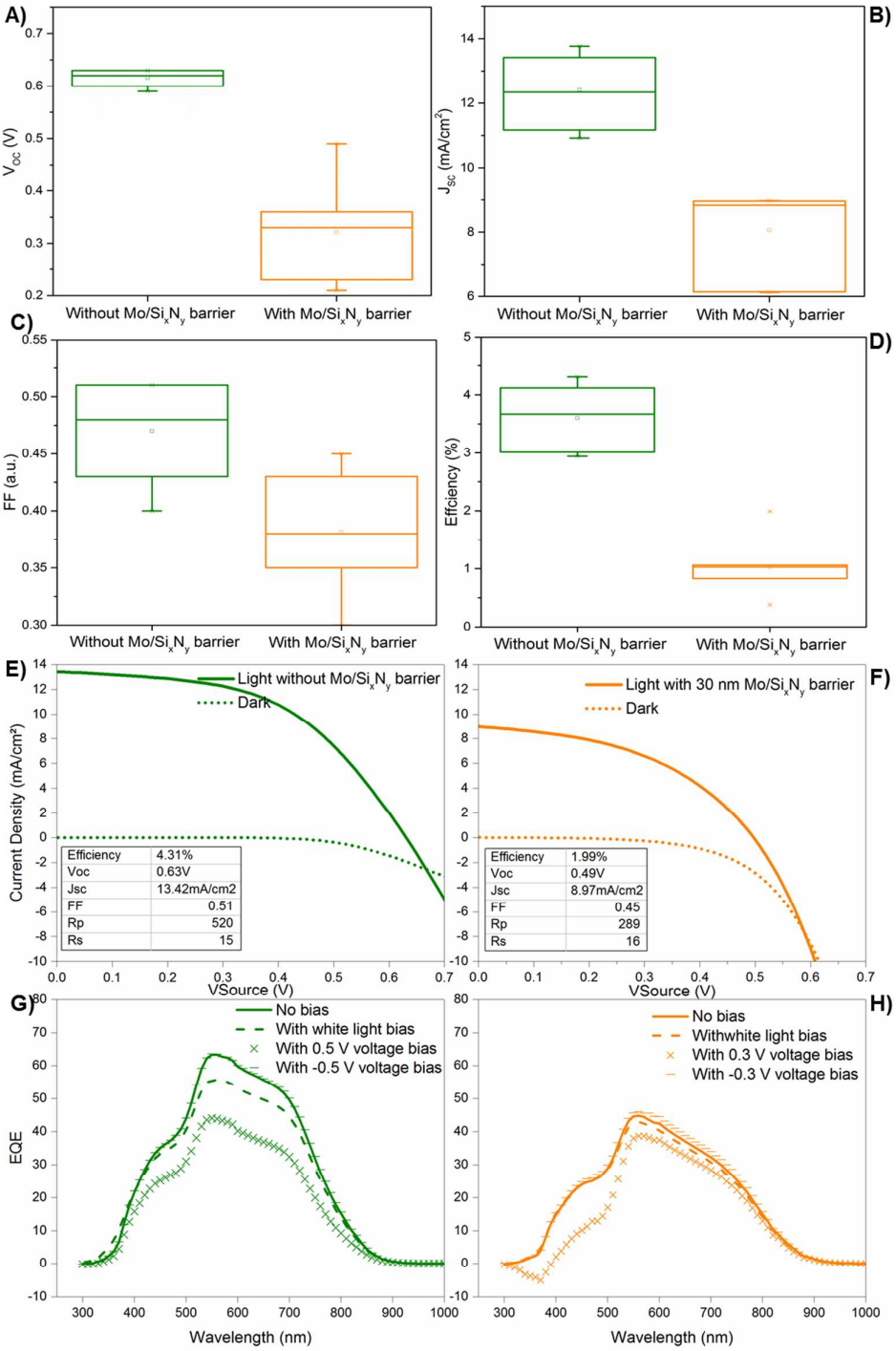

Figure 5. (A-D) Box charts of J-V characteristics of CZTS devices with and without Mo/Si_xN_y barrier layer. J-V curves for the best-performing CZTS solar cells fabricated E) without Mo/Si_xN_y barrier layers and F) with Mo/Si_xN_y barrier layers. Solid lines represent J-V curves under illumination and doted lines represent J-V curves in the dark condition. Basic device parameters were inserted in the graphs. EQE characteristics for the best-performing CZTS solar cells fabricated G) without Mo/Si_xN_y barrier layers and H) with Mo/Si_xN_y barrier layers under various bias conditions.

The 10 nm-, 20 nm- and 30 nm-Mo-capping/Si_xN_y/Mo/SLG stacks were used to fabricate CZTS devices and compared against the reference CZTS device directly deposited onto Mo/SLG. Unfortunately, most devices with Mo/Si_xN_y back contact showed a significant reduction in open-circuit voltage and short-circuit current as shown in Figure 5A-D. The highest efficiency of 1.99% was achieved with Mo-30 nm/Si_xN_y barrier layer (Figure 5F) with significant reduction in V_{oc} and J_{sc} along with some decrease in FF as compared to solar cells without barrier layers (Figure 5E). The cross-over behaviour between the light and dark *J-V* curve could be an indication of the presence of a blocking back contact at the interface between the Mo and CZTS.[26]

Light-bias-dependent and voltage-bias-dependent EQE were performed to investigate the efficiency loss mechanisms of fabricated CZTS solar cells as shown in Figure 5G and 5H. The minimum bandgap was estimated to be 1.58 eV and 1.54 eV from the absorption onset of EQE curves for the fabricated CZTS solar cells with and without barrier layers, respectively. Under white light bias (approximately 1 sun), no pronounced difference in the blue EQEs were observed for both samples as compared to that in the dark. This could be because the monochromatic blue probing beam has lower intensity than the blue part of the white bias light.[27] Thus it is hard to measure an increased EQE signal from charge carriers generated in the CdS region. However, noticeable drops in the wavelength range of 500 to 750 nm under illumination were seen compared to those in the dark. This reduction could be caused by the extra photogenerated electrons in the conduction band, which reduces the effective work function of CZTS and leads to lower collection efficiency. [28]

Voltage-bias-dependent EQE was used to create a forward bias and a reserve bias on the two devices. To avoid any damage caused by the bias voltage, the bias voltages (±0.5 V and ±0.3 V for the solar cell with and without Mo/Si_xN_y barrier layers) that were chosen are slightly lower than V_{oc} of two devices (Figure 5G and 5H). Compared to the EQE under no bias condition (in the dark), the EQE increases marginally at longer wavelength with applied -0.5 V (Figure 5G) and -0.3 V (Figure 5H) reverse voltage biases. This is mainly contributed by the increased depletion width in CZTS under reverse voltage bias which helps the collection efficiency of red photons.[27] This observation also indicates high recombination losses and low minority carrier lifetime within the p-type CZTS absorber layers.[28] This low lifetime could stem from a high defect concentration in the absorber layer or high recombination losses at the back contact or at the front interface.[26] The EQE decreases across the whole spectrum range with applied +0.5 V (Figure 5G) and +0.3 V (Figure 5H) forward voltage biases compared with the zero voltage bias. This could be because the depletion width in CZTS reduces significantly with forward voltage bias, hence a much lower carrier collection of photogenerated minority carriers.[29] It is notable that the negative EQE values were obtained at the wavelength between 300 nm and 400 nm under reverse bias of +0.3 V. Although applied forward voltage is still lower than V_{oc}, the dark current caused by majority carrier electrons in n-type CdS is larger than the photogenerated current, therefore an overall negative EQE is obtained. The reduced built-in electrical field also reduces the number of drift electrons moving towards the p-n junction.[28] The device with Mo/Si_xN_y barrier layers is

more sensitive to the reduction of depletion width, which could be partially caused by accumulation of holes at the Mo/Si_xN_y barrier layers.

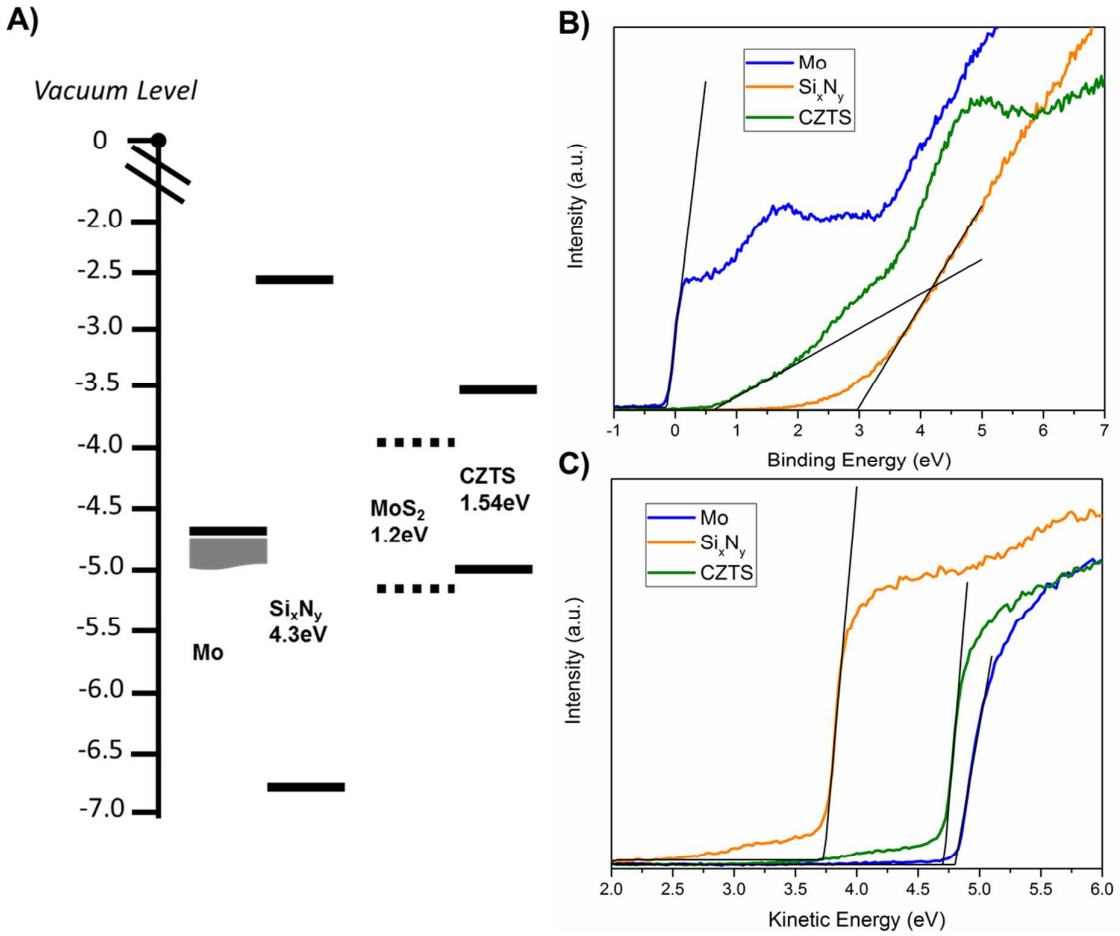

Figure 6. A) Band diagram of the effective band edge states of the CZTS and modified back contact layers in solid lines. B) the Fermi level and C) work functions are measured by UPS which were used to calculate the ionisation potential (or valence band maximum) of each film. The band gap of the CZTS and Si_xN_y were obtained using EQE and UV-VIS, respectively. Band edge states of the MoS_2 were adapted from reference [30], which could not be detected by UPS in this work.

To investigate differences in energetics after applying the Mo/Si_xN_y barrier layers, we employed ultraviolet photoelectron spectroscopy (UPS). Ionisation potentials (IP or valence band maximum of (6.8 ± 0.1) eV and (5.1 ± 0.1) eV were measured for Si_xN_y and CZTS films, respectively, as shown in Figure 6. Mo thin films were found to have a work function of (4.7 ± 0.1) eV. A 2 eV greater barrier height was introduced by 30 nm-thick Mo/Si_xN_y layers compared to unmodified CZTS. This difference would form a blocking back contact at the interface between the Mo and CZTS, which can suppress the majority carrier (hole) transport.

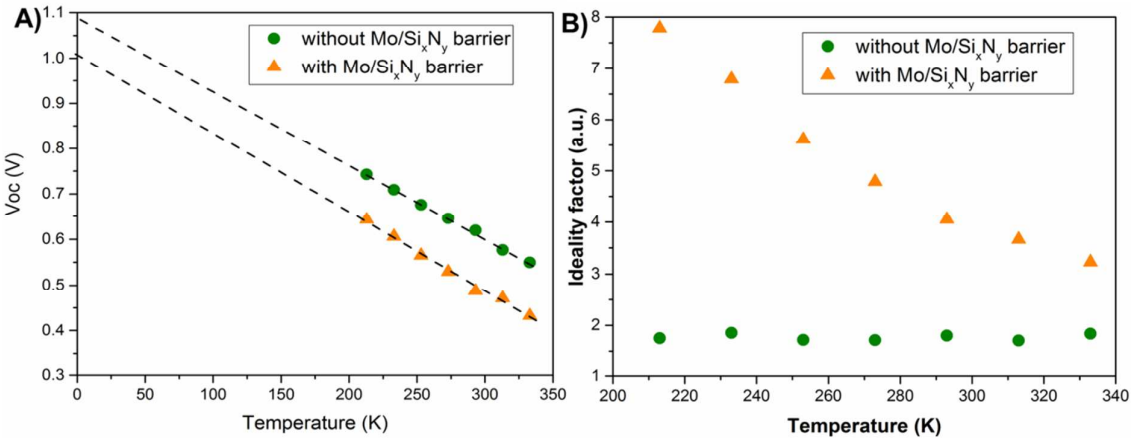

Figure 7. A) Temperature dependency of open-circuit voltage (V_{oc}) for CZTS solar cells without Mo/Si_xN_y barrier layers (solid circles) and with Mo/Si_xN_y barrier layers (solid triangles), the linear extrapolation to $T = 0$ K in dashed lines. Data for both devices have 0 K intercepts that do not reach the band gap value. B) The correlated ideality factors versus temperature data for without Mo/Si_xN_y barrier layers (solid circles) and with Mo/Si_xN_y barrier layers (solid triangles).

To further investigate the deficiency of the performance of the CZTS device with a Mo/Si_xN_y barrier as compared with the CZTS device without this barrier, temperature dependent V_{oc} data has been collected to determine the dominant recombination processes. The relationship between V_{oc} and temperature is according to [31] and as shown below:

$$V_{OC} = \frac{E_a}{q} - \frac{AkT}{q} ln \frac{J_{00}}{J_L} \qquad \text{Equation 2}$$

where E_a, A, J_{00}, J_L, q, k and T are the activation energy for dominant recombination mechanism, diode ideality factor, reverse saturation current prefactor, photocurrent, electron charge, Boltzmann constant and the temperature, respectively. The V_{oc} vs T plots are shown in Figure 7A for the CZTS devices with and without Mo/Si_xN_y barrier layers, which yield 0 K intercept of the linear extrapolation of E_a/q values of 1.08 and 1.01 eV, respectively. Those E_a/q values are low compared to their respective band gap values (1.58 and 1.54 eV) which obtained from EQE measurement. This result indicates that the main recombination mechanism in these CZTS cells is dominated by interface recombination.[26] The more pronounced reduction on E_a/q value of the CZTS cell with the Mo/Si_xN_y barrier layers could be due to increased interface recombination occurring at the back contact with improper band alignment (Figure 7A). The efficiency for both devices collapses at low temperature due to increasing series resistance and the possible charge carrier freeze-out effect at low temperature as agreed with other publications.[26, 32] In Figure 7B, the T-dependent diode ideality factors for both CZTS solar cells with and without Mo/Si_xN_y barrier layers were plotted. The diode ideality factors for the CZTS solar cell without the Mo/Si_xN_y barrier are between 1 and 2, showing a marginal variation in the measured temperature range, which could be an indication of the deep defects acting as dominant trap states or so called Shockley-Read-Hall recombination via band tails.[27, 33] However, a significant increase of

diode ideality factor (A>2) was observed for CZTS solar cells with the Mo/Si_xN_y barrier at low temperatures. The origin of A>2 is not only by considering a single recombination route, but involves a multistep recombination process via a series of trap states distributed within the solar cell device structure. [34] This would indicate strong back contact recombination which could lower V_{oc}.[26, 34-35]

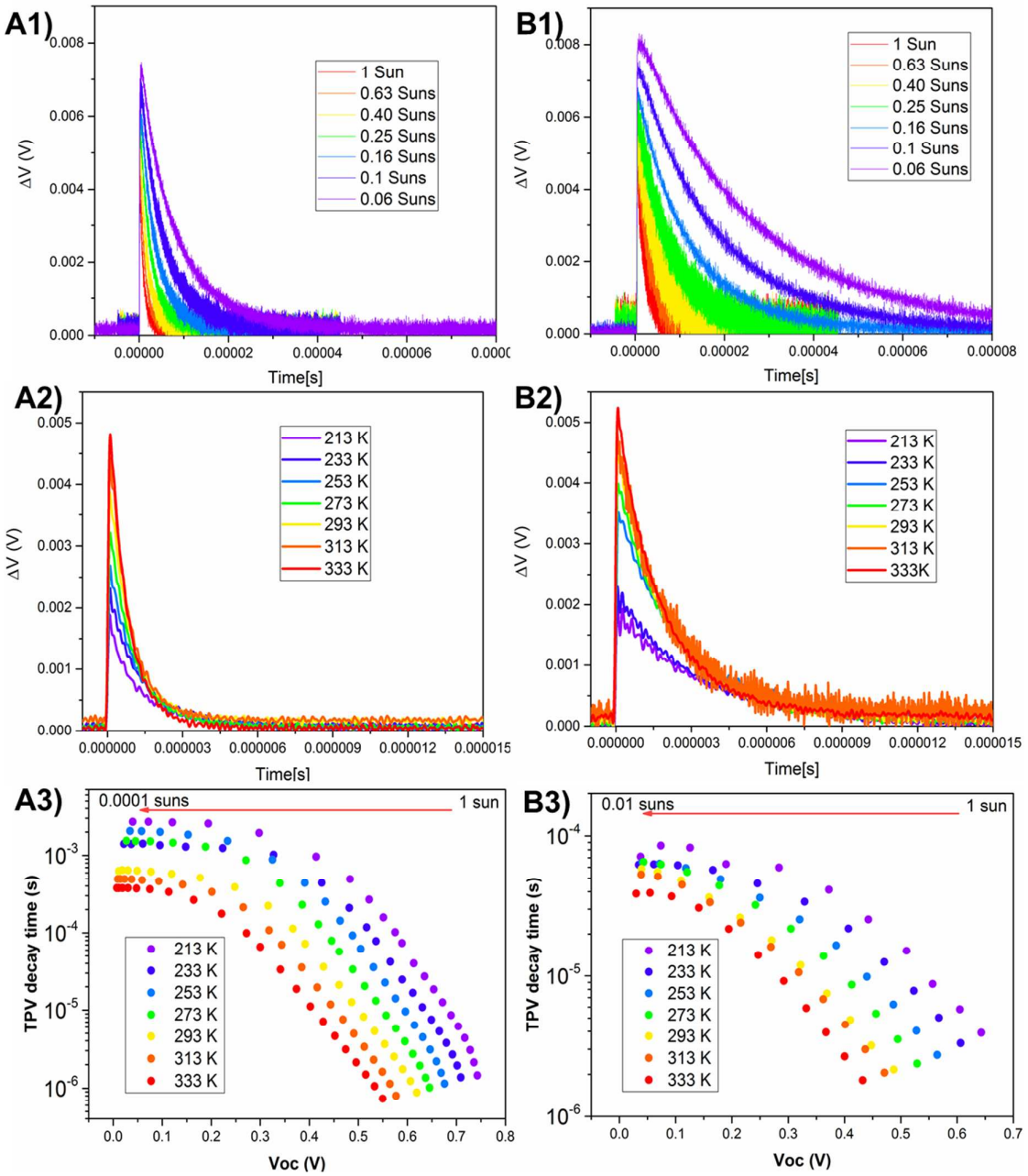

Figure 8. The representative TPV decays analysis of CZTS solar cells without Mo/Si_xN_y barrier layers (A) and with Mo/Si_xN_y barrier layers (B). A1) and B1) The representative TPV decay as a function of white-light bias in the range of 0.06 - 1 suns at 293 K. A2) and B2) Temperature-dependent TPV decay under 1 sun white-light bias at the temperature range of 213 – 333 K. A3) and B3) TPV decay time characteristics of CZTS solar cells under WLB range of 0.0001 – 1 suns and temperature range of 213 – 333 K.

To understand how the charge transport behaviour at the CZTS/back contact interface differs between the device types, we conducted temperature-dependent TPV measurements. For TPV measurements, a light pulse is applied to a device held at open-circuit condition under a white-light bias (WLB), and the resulting photovoltage changes created by the laser pulse (ΔV) is measured over time. From this, we measured the decay time of the open-circuit voltage as a function of the intensity of WLB, shown in Figure 8A1 and 8B1. TPV decay measurement gives insight into the internal recombination dynamics of the charge carriers. The decay time represents the internal extraction time to the contracts of the charge carriers before they recombine or are trapped in the defects.[36] The longer decay time measured, the higher chance the photo-generated charge carriers can be extracted. The decay times of charge carriers for the CZTS solar cells with and without Mo/Si_xN_y barrier layers are estimated on the order of ~μs in the WLB range of 0.06 – 1 suns. With increasing WLB, V_{oc} of both CZTS devices increases. This could be caused by shallow defects that were fulfilled at higher excitation densities.[37] By increasing the WLB, there are more photo-generated minority charge carriers (electrons) in the CZTS absorber which could also increase the internal recombination with holes, reducing the extraction time. The variation on decay time of CZTS with Mo/Si_xN_y barrier layers using different light intensities is more significant than the CZTS device without the Mo/Si_xN_y barrier layers. This would be a sign of stronger recombination caused by this modified back contact. To investigate the thermally activated charge transport, temperature dependent TPV decay for the CZTS solar cells with and without Mo/Si_xN_y barrier layers at different temperature under 1 sun WLB were shown in Figure 8A2 and 8B2. The decay time of both CZTS devices increases with decreasing temperature. The longer extraction time could be due to reduced thermal energy to assist the charge carrier to jump spatially over fluctuated electrostatic potential [7] and travel across the CZTS device. A more pronounced variation on ΔV and decay time for CZTS device with Mo/Si_xN_y barrier layers at different temperature as compared to the CZTS device without the barrier layers was obtained. To find out the combined effects of the intensity of WLB and temperature on TPV decay time, TPV decay time versus V_{oc} at different conditions were shown in Figure 8A3 and 8B3. The data were recorded until $V_{oc} \sim 0$ at lowest light levels of WLB. We could still obtain V_{oc} at even 0.0001 suns for the CZTS solar cell device without Mo/Si_xN_y barrier layers, which is nearly 100 times lower light intensity than for CZTS device with Mo/Si_xN_y barrier layers. In other words, the increased interfacial recombination in the cell with Mo/SiN causes a significant decrease in V_{oc} at low light intensities. The TPV signal decays 100 times faster for a given V_{oc} after introducing the Mo/Si_xN_y barrier into device structure. These results indicate that the recombination within the CZTS device with Mo/Si_xN_y barrier layers may not only account for trapping and detrapping process[38], but can also be attributed to the increased interface recombination between accumulated holes near the high barrier layer and free electrons in CZTS. This is in good agreement with the hole blocking effect observed from temperature dependent *J-V* measurement.

CONCLUSIONS

In conclusion, we have engineered Mo/Si_xN_y barrier layers into a back contact structure for CZTS solar cells to effectively reduce the formation of the detrimental MoS_2 layer, which

was revealed by EDS mapping on the cross-section of CZTS samples with and without Mo/Si_xN_y barrier layers. We also demonstrated that stress measurements can be used to monitor the dramatic changes after the addition of every back contact layers, providing empirical guidance to control the adhesion of these films. A power conversion efficiency drop of 2.32% was observed after introducing the modified back contact. This reduction of efficiency is mainly due to the increased recombination towards back contact, which stem from the misalignment of valence band maximum between Si_xN_y and CZTS obtained by UPS. We have also demonstrated a combination characterisation methods to reveal the recombination information within the CZTS solar cells, particularly temperature dependent J-V and TPV showed an increased in interface recombination and poor hole extraction due to misalignment of band edges between Mo/Si_xN_y/CZTS region.

ACKNOWLEDGMENTS

This work was funded by Engineering and Science Research Council (EPSRC): EP/L017792/1: Photovoltaic Technology Based on Earth-Abundant materials (PVTeam). T.D. and J.S. would thank to Sêr Cymru National Research Network in Advanced Engineering and Materials (NRN-072). A. P. and M. J. C. thank: the British Council for funding, through the Newton Al-Farabi Partnership; and the European Regional Development Fund (ERDF) and the Welsh European Funding Office (WEFO) for funding the 2nd Solar Photovoltaic Academic Research Consortium (SPARC II). The authors would thank Dr. Peter Greenwood from Swansea University for the graphic design help.

REFERENCES

(1) Yan, C.; Sun, K.; Huang, J.; Johnston, S.; Liu, F.; Veettil, B. P.; Sun, K.; Pu, A.; Zhou, F.; Stride, J. A.; Green, M. A.; Hao, X. Beyond 11% Efficient Sulfide Kesterite $Cu_2Zn_xCd_{1-x}SnS_4$ Solar Cell: Effects of Cadmium Alloying. *ACS Energy Lett.* **2017,** *2*, 930-936.
(2) Su, Z.; Tan, J. M. R.; Li, X.; Zeng, X.; Batabyal, S. K.; Wong, L. H. Cation Substitution of Solution-Processed Cu_2ZnSnS_4 Thin Film Solar Cell with over 9% Efficiency. *Adv. Energy Mater.* **2015,** *5*, 1500682.
(3) Ericson, T.; Larsson, F.; Törndahl, T.; Frisk, C.; Larsen, J.; Kosyak, V.; Hägglund, C.; Li, S.; Platzer-Björkman, C. Zinc-Tin-Oxide Buffer Layer and Low Temperature Post Annealing Resulting in a 9.0% Efficient Cd-Free Cu_2ZnSnS_4 Solar Cell. *Sol. RRL* **2017,** *1* , 1700001.
(4) Tajima, S.; Umehara, M.; Hasegawa, M.; Mise, T.; Itoh, T. Cu_2ZnSnS_4 Photovoltaic Cell with Improved Efficiency Fabricated by High-Temperature Annealing after CdS Buffer-Layer Deposition. *Prog. Photovolt: Res. Appl.* **2017,** *25*, 14-22.
(5) Wang, W.; Winkler, M. T.; Gunawan, O.; Gokmen, T.; Todorov, T. K.; Zhu, Y.; Mitzi, D. B. Device Characteristics of CZTSSe Thin-Film Solar Cells with 12.6% Efficiency. *Adv. Energy Mater.* **2014,** *4*, 1301465.
(6) Scragg, J. J.; Wätjen, J. T.; Edoff, M.; Ericson, T.; Kubart, T.; Platzer-Björkman, C. A Detrimental Reaction at the Molybdenum Back Contact in $Cu_2ZnSn(S,Se)_4$ Thin-Film Solar Cells. *J. Am. Chem. Soc.* **2012,** *134*, 19330-19333.
(7) Gokmen, T.; Gunawan, O.; Todorov, T. K.; Mitzi, D. B. Band Tailing and Efficiency Limitation in Kesterite Solar Cells. *Appl. Phys. Lett.* **2013,** *103*, 103506.
(8) Shin, B.; Zhu, Y.; Bojarczuk, N. A.; Chey, S. J.; Guha, S. Control of an Interfacial $MoSe_2$ Layer in $Cu_2ZnSnSe_4$ Thin Film Solar Cells: 8.9% Power Conversion Efficiency with a TiN Diffusion Barrier. *Appl. Phys. Lett.* **2012,** *101*, 053903.

(9) Liu, F.; Sun, K.; Li, W.; Yan, C.; Cui, H.; Jiang, L.; Hao, X.; Green, M. A. Enhancing the Cu_2ZnSnS_4 Solar Cell Efficiency by Back Contact Modification: Inserting a Thin TiB_2 Intermediate Layer at Cu_2ZnSnS_4/Mo Interface. *Appl. Phys. Lett.* **2014,** *104*, 051105.
(10) Puvaneswaran, C.; Mohammad Istiaque, H.; Jamilah, H.; Mohammad, A.; Kamaruzzaman, S.; Nowshad, A. Effects of Transition Metal Dichalcogenide Molybdenum Disulfide Layer Formation in Copper–Zinc–Tin–Sulfur Solar Cells from Numerical Analysis. *Jpn. J. Appl. Phys.* **2012,** *51*, 10NC32.
(11) Cui, H.; Lee, C.-Y.; Li, W.; Liu, X.; Wen, X.; Hao, X. Improving Efficiency of Evaporated Cu_2ZnSnS_4 Thin Film Solar Cells by a Thin Ag Intermediate Layer between Absorber and Back Contact. *Int. J. Photoenergy* **2015,** *2015*, 9.
(12) Lopez-Marino, S.; Espíndola-Rodríguez, M.; Sánchez, Y.; Alcobé, X.; Oliva, F.; Xie, H.; Neuschitzer, M.; Giraldo, S.; Placidi, M.; Caballero, R.; Izquierdo-Roca, V.; Pérez-Rodríguez, A.; Saucedo, E. The Importance of Back Contact Modification in $Cu_2ZnSnSe_4$ Solar Cells: The Role of a Thin MoO_2 layer. *Nano Energy* **2016,** *26*, 708-721.
(13) Li, W.; Chen, J.; Cui, H.; Liu, F.; Hao, X. Inhibiting MoS_2 Formation by Introducing a ZnO Intermediate Layer for Cu_2ZnSnS_4 Solar Cells. *Materials Letters* **2014,** *130*, 87-90.
(14) Lopez-Marino, S.; Espíndola-Rodríguez, M.; Sánchez, Y.; Alcobé, X.; Oliva, F.; Xie, H.; Neuschitzer, M.; Giraldo, S.; Placidi, M.; Caballero, R.; Izquierdo-Roca, V.; Pérez-Rodríguez, A.; Saucedo, E. The Importance of Back Contact Modification in $Cu_2ZnSnSe_4$ Solar Cells: The Role of a Thin MoO_2 layer. *Nano Energy* **2016,** *26*, 708-721.
(15) Blösch, P.; Nishiwaki, S.; Jaeger, T.; Kranz, L.; Pianezzi, F.; Chirilă, A.; Reinhard, P.; Buecheler, S.; Tiwari, A. N. Alternative Back Contact Designs for $Cu(In,Ga)Se_2$ Solar Cells on Polyimide Foils. *Thin Solid Films* **2013,** *535*, 220-223.
(16) Scragg, J. J.; Kubart, T.; Wätjen, J. T.; Ericson, T.; Linnarsson, M. K.; Platzer-Björkman, C. Effects of Back Contact Instability on Cu_2ZnSnS_4 Devices and Processes. *Chem. Mater.* **2013,** *25*, 3162-3171.
(17) Colina, M.; Martín, I.; Giraldo, S.; Sánchez-González, Y.; Kondrotas, R.; Oliva, F.; Izquierdo-Roca, V.; Pérez-Rodríguez, A.; Coll, A.; Alcubilla, R.; Saucedo, E. Influence of Amorphous Silicon Carbide Intermediate Layer in the Back-Contact Structure of $Cu_2ZnSnSe_4$ Solar Cells. *IEEE Journal of Photovoltaics* **2016,** *6*, 1327-1332.
(18) Antunez, P. D.; Bishop, D. M.; Lee, Y. S.; Gokmen, T.; Gunawan, O.; Gershon, T. S.; Todorov, T. K.; Singh, S.; Haight, R. Back Contact Engineering for Increased Performance in Kesterite Solar Cells. *Adv. Energy Mater.* **2017**, *7*, 1602585.
(19) Riley, F. L. Silicon Nitride and Related Materials. *J. Am. Chem. Soc.* **2000,** *83*, 245-265.
(20) Wan, Y.; McIntosh, K. R.; Thomson, A. F. Characterisation and Optimisation of PECVD SiN_x as an Antireflection Coating and Passivation Layer for Silicon Solar Cells. *AIP Advances* **2013,** *3*, 032113.
(21) Elowe, P. R.; Stempki, M. A.; Rozeveld, S. J.; DeGroot, M. W. Development of Direct Cell Inorganic Barrier Film Technology Providing Exceptional Device Stability for CIGS Solar Cells. *Chem. Mater.* **2011,** *23*, 3915-3920.
(22) Wei, Z.; Zhu, M.; McGettrick, J. D.; Kissling, G. P.; Peter, L. M.; Watson, T. M. The effect of Additional Sulfur on Solution-Processed Pure Sulfide Cu_2ZnSnS_4 Solar Cell Absorber Layers. *MRS Advances* **2016,** *FirstView*, 1-6.
(23) Day, J. C. C. http://www.daytasystems.co.uk.
(24) Malerba, C.; Valentini, M.; Azanza Ricardo, C. L.; Rinaldi, A.; Cappelletto, E.; Scardi, P.; Mittiga, A. Blistering in Cu_2ZnSnS_4 thin films: correlation with residual stresses. *Materials & Design* **2016,** *108*, 725-735.
(25) Fitzpatrick, M. E.; Fry, A. T.; Holdway, P.; Kandil, F. A.; Shackleton, J.; Suominen, L. *Determination of Residual Stresses by X-ray Diffraction – Issue 2*; **2005**.

(26) Mitzi, D. B.; Gunawan, O.; Todorov, T. K.; Wang, K.; Guha, S. The Path Towards a high-Performance Solution-Processed Kesterite Solar Cell. *Sol. Energy Mater. Sol. Cells* **2011,** *95*, 1421-1436.
(27) Hegedus, S. S.; Shafarman, W. N. Thin-Film Solar Cells: Device Measurements and Analysis. *Prog. Photovolt: Res. Appl.* **2004,** *12*, 155-176.
(28) Liu, F.; Yan, C.; Sun, K.; Zhou, F.; Hao, X.; Green, M. A. Light-Bias-Dependent External Quantum Efficiency of Kesterite Cu_2ZnSnS_4 Solar Cells. *ACS Photonics* **2017,** *4*, 1684-1690.
(29) Sze, S. M.; Ng, K. K. *Physics of Semiconductor Devices*, Third ed.; Hohn Wiley & Sons, Inc.: **2007**.
(30) Dhakal, T. P.; Harvey, S.; van Hest, M.; Teeter, G., Back Contact Band Offset Study of Mo-CZTS Based Solar Cell Structure by Using XPS/UPS Techniques. In *2015 IEEE 42nd Photovoltaic Specialist Conference (PVSC)*, New Orleans, **2015**, 1-4.
(31) Nadenau, V.; Rau, U.; Jasenek, A.; Schock, H. W. Electronic Properties of $CuGaSe_2$-based Heterojunction Solar Cells. Part I. Transport Analysis. *Journal of Applied Physics* **2000,** *87*, 584-593.
(32) Todorov, T. K.; Tang, J.; Bag, S.; Gunawan, O.; Gokmen, T.; Zhu, Y.; Mitzi, D. B. Beyond 11% Efficiency: Characteristics of State-of-the-Art $Cu_2ZnSn(S,Se)_4$ Solar Cells. *Adv. Energy Mater.***2013,** *3*, 34-38.
(33) Berkel, C. v.; Powell, M. J.; Franklin, A. R.; French, I. D. Quality Factor in a-Si:H nip and Pin Diodes. *J. Appl. Phys.***1993,** *73*, 5264-5268.
(34) Rau, U. Tunneling-Enhanced Recombination in $Cu(In,Ga)Se_2$ Heterojunction Solar Cells. *Appl. Phys. Lett.* **1999,** *74*, 111-113.
(35) Gunawan, O.; Gokmen, T.; Mitzi, D. B. Suns-VOC Characteristics of High Performance Kesterite Solar Cells. *J. Appl. Phys.* **2014,** *116*, 084504.
(36) Lin, W. M. M.; Bozyigit, D.; Yarema, O.; Wood, V. Transient Photovoltage Measurements in Nanocrystal-Based Solar Cells. *J. Phys. Chem. C* **2016,** *120*, 12900-12908.
(37) Halpert, J. E.; Morgenstern, F. S. F.; Ehrler, B.; Vaynzof, Y.; Credgington, D.; Greenham, N. C. Charge Dynamics in Solution-Processed Nanocrystalline $CuInS_2$ Solar Cells. *ACS Nano* **2015,** *9*, 5857-5867.
(38) Hages, C. J.; Redinger, A.; Levcenko, S.; Hempel, H.; Koeper, M. J.; Agrawal, R.; Greiner, D.; Kaufmann, C. A.; Unold, T. Identifying the Real Minority Carrier Lifetime in Nonideal Semiconductors: A Case Study of Kesterite Materials. *Adv. Energy Mater.* **2017,** *7*, 1700167.

For Table of Contents Only

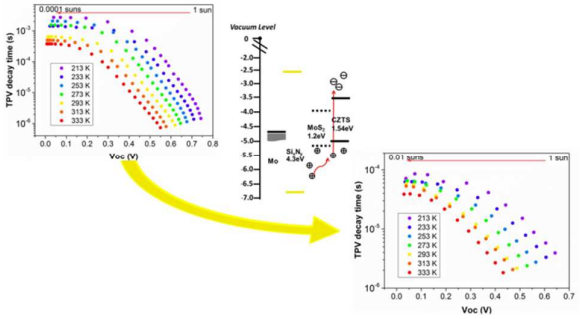

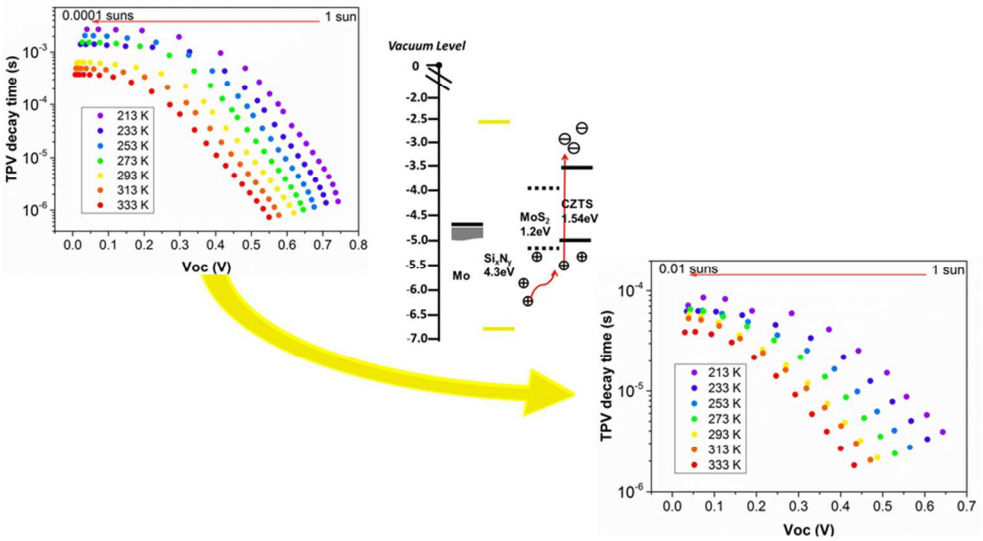

For Table of Contents Only

82x44mm (300 x 300 DPI)